SAND2016-5293C

IN SITU TEM OBSERVATIONS OF CORROSION IN NANOCRYSTALLINE Fe THIN FILMS

David Gross[1], Josh Kacher[2], Khalid Hattar[3], Ian M. Robertson[1]
[1]University of Wisconsin-Madison, 1415 Engineering Dr., Madison, WI 53706
[2]Georgia Institute of Technology, Atlanta, GA
[3]Sandia National Laboratories, Albuquerque, NM
Key words: Corrosion; Transmission Electron Microscopy; Nanocrystalline

Abstract

The corrosion of pulsed-laser deposited Fe thin films by aqueous acetic acid solution was explored in real time by performing dynamic microfluidic experiments *in situ* in a transmission electron microscope. The films were examined in both the as-deposited condition and after annealing. In the as-deposited films, discrete events featuring the localized dissolution of grains were observed with the dissolved volumes ranging in size from ~1.5 x 10^{-5} μm^3 to 3.4 x 10^{-7} μm^3. The annealed samples had larger grains than the as-deposited samples, were more resistant to corrosion, and did not show similar discrete dissolution events. The electron beam was observed to accelerate the corrosion, especially on the as-deposited samples. The effects of grain surface energy, grain boundary energy and the electron beam-specimen interactions are discussed in relation to the observed behavior.

Introduction

Fe is protected from corrosion by the formation of a passive oxide layer [1-7]. This layer isolates underlying iron from the solution preventing dissolution. The passive film in Fe is a complex spinel structure, related to but distinct from γ-Fe_2O_3 and Fe_3O_4 [5, 7], that can potentially include iron hydroxide compounds and adsorbed water [2]. This passivation layer has been observed to vary in defect concentration, making it more strongly protective in certain places than others [5]. This paper reports the observation of the dynamics of corrosion of nanocrystalline Fe by conducting corrosion experiments *in situ* via transmission electron microscopy (TEM) using a microfluidic cell. By flowing a corrosive liquid through the microfluidics of the stage, effects of corrosion and the mechanisms by which film breakdown and sample dissolution occur can be observed directly.

Previous efforts to observe corrosion events in the TEM have included *post mortem* corrosion characterization [8-10], *in situ* characterization in a gaseous environment [11-13], and *in situ* liquid cell corrosion of Al and Cu thin films [14]. The *in situ* studies all found that the corrosion was a localized event, with Zhou *et al*. finding that copper undergoing oxidation at high temperatures exposed to air nucleated copper islands which then grew to form the oxide scale [11, 12]. Malladi *et al*. found that for Al-2024 exposed to gaseous HCl, the corrosion was localized primarily to defects in the material, including precipitates acting as the cathodic sites to stimulate corrosion [13]. Chee *et al.* flowed an aqueous NaCl solution over Al and Cu thin films while applying a bias to encourage active corrosion events. They found that the corrosion generally proceeded via film pitting, connected corrosion pathways, and blistering. Exposure of the films to the electron beam was found to accelerate the corrosion events, though comparison to films corroded *ex situ* showed similar corrosion features, suggesting that the electron beam

influenced the corrosion rate, but not necessarily the corrosion mechanisms. Possible influences of electron beam irradiation during corrosion include: radiolysis of water [15-17], heating due to the electron beam [15, 16, 18], chemical reaction initiation [15], and charge collection [17, 18]. This paper explores the corrosion processes occurring during flow of an aqueous acetic acid solution over high-purity nanocrystalline Fe thin films.

Methodology

A microfluidic TEM stage manufactured by Protochips, Inc. was used to investigate in real time the corrosion of a pulsed laser deposited Fe film by a 20% acetic acid solution. Two Si chips with amorphous Si_3N_4 windows were used to enable electron transparency, while containing the liquid. Pulsed laser deposition (PLD) was used to deposit the film directly onto Si chips using a KrF laser with a wavelength of 248 nm, a pulse width of 34 ns full-width half-maximum, a pulse rate of 35 Hz, and an energy density at the target of 1-2 J/cm^2. A total of 7,587 pulses was used to achieve a nominal film thickness of 50.3 nm with the film growing at a rate of 0.23 nm/s. Acetic acid was chosen because it was compatible with the microfluidics of the stage, while still being corrosive to Fe. The 20% solution was selected as studies of on corrosion of stainless steel suggest that this composition maximizes corrosion-susceptibility [19, 20]. Two samples were annealed post-deposition under vacuum at 400°C to induce grain growth.

Prior to assembly of the stage, deionized water was pumped through the microfluidics to remove contaminants. The stage was then assembled and cleaned using deionized water and leak checked prior to insertion in to a JEOL 2100 LaB_6 TEM. Samples were observed under bright-field conditions at an accelerating voltage of 200 keV. During TEM observation, the fluid was switched from deionized water to a 20% acetic acid solution with a flow rate of 100 μL/hr. Corrosion of the nanocrystalline matrix was recorded continuously to capture the relatively rapid corrosion events. Movie frames were obtained using a TVIPS Fast-Scan F114 operating at 1024x1024 pixels. In the annealed materials, snapshots of the films were collected periodically with the beam blanked between images to reduce electron beam exposure. Still images and diffraction patterns were obtained by a TVIPS TemCam-F416 operating at 4096x4096 pixels. Image analysis and adjustments were performed using Adobe Photoshop CS6 and ImageJ.

Results

The corrosion behavior of the as-deposited films was observed to occur in two different ways: short (< 0.5 s) events of localized dissolution and rapid, large scale propagation of corrosion fronts. Figures 1-2 show the former behavior and Figure 3 shows the latter. The bright-field micrograph presented in Figure 1A shows the as-deposited microstructure after brief exposure to acetic acid. The initial microstructure was composed of a nanocrystalline Fe matrix with an average grain size of approximately 20 nm as determined by the line intercept method. Selected area diffraction analysis showed that the film had little to no preferred texture (Fig. 1A inset). Several areas are circled in Figure 1A indicating where dissolution had occurred prior to imaging. Figure 1B shows the state of the area following 35 s of continuous imaging during acetic acid flow. The three areas circled remained unchanged, but additional through-thickness pits in the film formed. Each of these additional pits is discrete and isolated from the other pits. For example, the two pits indicated by the arrow in Figure 1B are nearly overlapping, but formed at different times and are subsequently separated by a thin ligament of material. This small

ligament appears to be relatively stable despite its small mass and being surrounded by acidic solution on three sides. The observed dissolution events during this cycle resulted in stable, corroded regions with diameters ranging from 70 to 100 nm. The volume consumed in each event, assuming a constant film thickness of 50 nm, ranged from 60,000 nm^3 to 320,000 nm^3 per event with an average of 190,000 nm^3. Assuming the room temperature density of iron of 7.87 g/cm^3 [21] is valid, the mass loss ranged from 0.47 femtograms to 2.5 femtograms with an average loss of 1.5 femtograms. The total volume corroded was approximately 3.2 x 10^{-3} μm^3 or 25 femtograms of material, which is approximately 3% of the imaged volume and mass. A video of the corrosion behavior can be seen at: http://www.youtube.com/watch?v=f0k6C7nKrFo.

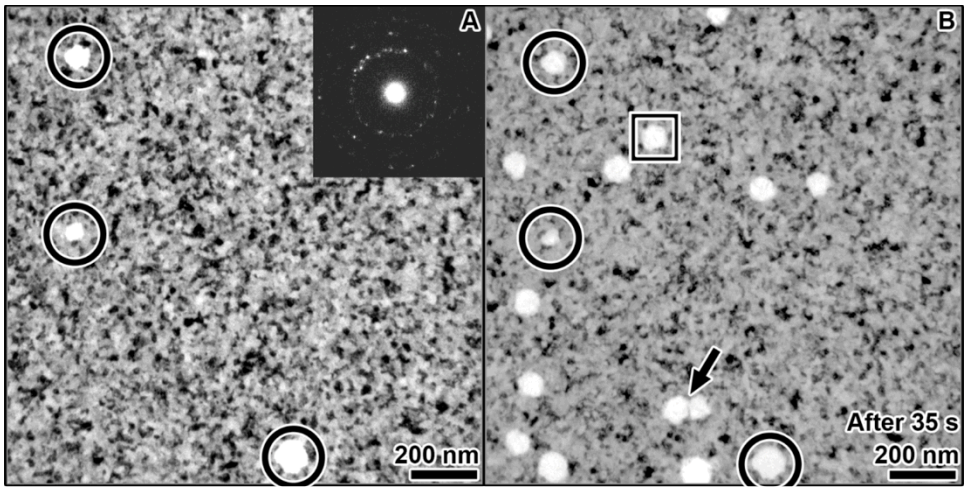

Figure 1: Bright field TEM micrographs captured from individual still frames. A shows the initial state and B shows the microstructure after 35s of exposure. Pits present before exposure are circled in both A and B. The arrow in B highlights a thin segment of material separating two distinct corrosion events. The squared region is explored in further detail in Fig. 2.

The initiation and growth of a corrosion site, highlighted by a square in Figure 1B, is shown in the series of time resolved bright-field images presented in Figure 2. The initial state of the area, Figure 2A, shows one previously corroded region; the encircled area captures the region of further corrosion although this site could not be selected *a priori*. Figure 2B-2F shows the dissolution occurring within the circled region; early indications of an event are the changes in contrast of some grains in the center of the circle. The corroded region expanded to consume the surrounding grains, with approximately 8 grains total corroded. The dark grain highlighted by an arrow in Figure 2C remained unaffected as the corrosive front progresses, suggesting local microstructural heterogeneity significantly influences the susceptibility to corrosion. The entire event demonstrated the dissolution of a total volume of 130,000 nm^3 for a total mass loss of 1.0 femtograms in approximately 0.36 s.

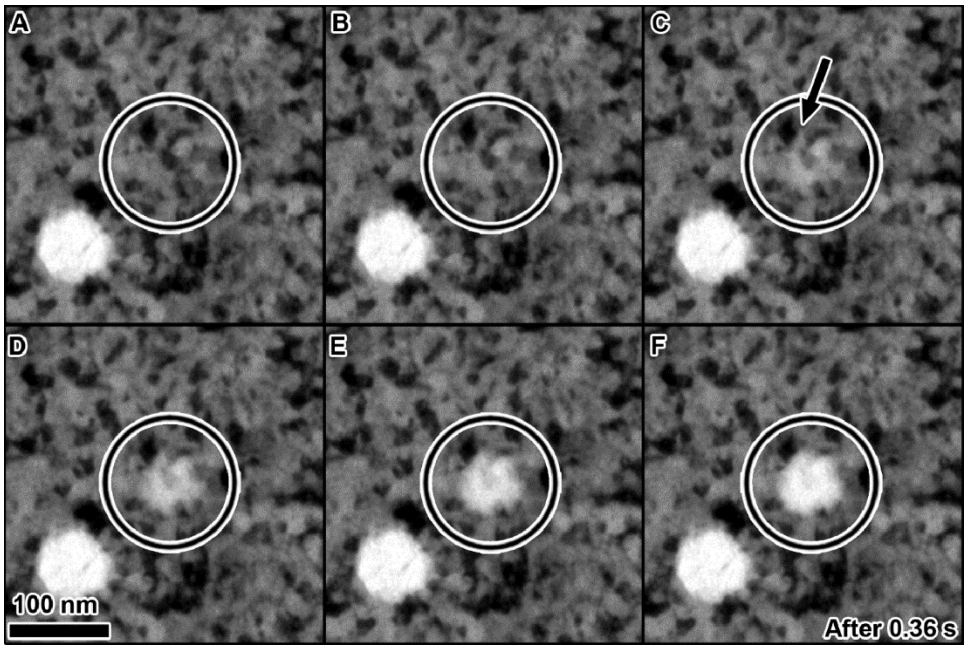

Figure 2: A time lapse series of micrographs detailing one corrosion event. Each image represent one frame from a video recorded at 13.75 frames per second. The evidence of dissolution can be seen by the change of contrast beginning in B that gradually spread through grains surrounding the sample. The dark grain in the center, indicated by an arrow in C, appears to be more resistant to corrosion.

While Figure 2 details the corrosion process most commonly seen in the as-deposited film, larger scale corrosion events also occurred. Figure 3, a series of time resolved bright-field images, displays a large scale corrosion event that shares some similarities with the event represented Figure 2. This event, and others similar to it, occurred after approximately 30 minutes of continuous acid exposure. In the lower portion of Figure 3A, significant film dissolution is seen, as well as a local contrast change, suggesting the initiation of an additional corrosion event; this site is circled. This dissolution occurred previous to any electron beam exposure. During continuous imaging, the corrosion front progressed rapidly in the highlighted region to a diameter of 450 nm with all of the grains contained within the corrosion front dissolved completely (Fig. 3B). The corroded region remained a near-circular shape, suggesting curvature-driven expansion. However, with further expansion, the corrosion front began expanding heterogeneously, suggesting the influence of factors other than curvature (Fig. 3C-D). An example of this is highlighted in Figure 3D where one segment of the expanding corrosion front is seen to expand much faster than the rest. Indeed, several grains remain unaffected by the corrosive environment even after the corrosion of all surrounding grains. The total volume consumed by this event is approximately 3.4×10^{-2} μm^3 with a total mass loss of 270 femtograms. The full video of the corrosion event can be viewed online at: http://www.youtube.com/watch?v=x7gR8-HRwJw.

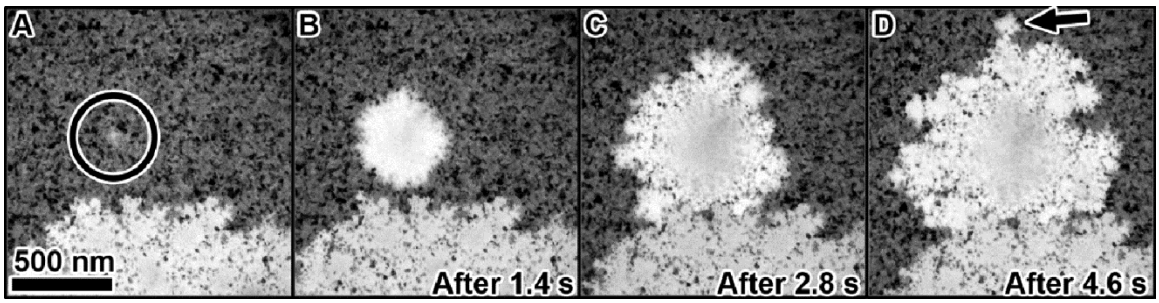

Figure 3: Growth of a large scale dissolution event. The circle in A highlights the initiation of a corrosion event and the arrow in D shows an example of non-curvature driven growth.

As with all *in situ* TEM experiments there is a question about the influence of the electron beam on the liquid-specimen interactions. Here, it was found that the electron beam accelerated the reaction rate as multiple experiments could be performed in the same film by moving to a new area. The size and morphology of the pitted structure appear similar with and without prior electron beam exposure, as seen in both Figures 1 and 3. No interrupted exposure experiments were performed to delineate whether the electron beam affected nucleation, growth, or both rates due to the rapid propagation of the corrosion fronts in the as-deposited films.

To determine the effect of the grain boundary conditions and grains on the corrosion rate, some samples were annealed prior to exposure to the corrosive environment. Annealing caused general coarsening and some abnormal grain growth. An example of the resulting microstructure is shown in Figure 4A where the average grain size has increased to approximately 50 nm in diameter. This measurement excludes the abnormal grain, which has a diameter of approximately 400 nm. The material on the right side of Figure 4A corroded before any electron beam exposure. The micrographs presented in Figure 4 show the continuation of this corrosion event over 25 minutes with an image captured every 5 minutes; in this case the beam was blanked between images to minimize electron beam effects. The time resolved images show that the grains adjoining the abnormal grain were attacked preferentially over the surrounding matrix. Throughout the corrosion process, the large grain retained its original morphology, suggesting that it was insensitive to the corrosive medium, at least in the observed time frame. This was true even of small protrusions from the grain, one of which is highlighted in Figure 4A, whose high surface area to volume ratio would expectedly make them especially susceptible to corrosion. The corrosion rate was much slower than what was observed in the as-deposited films, with a total volume consumed of 1.75×10^{-3} μm^3 and a total mass consumed of 14 femtograms over 25 minutes, which is greater than a 50 fold decrease from the corrosion rate for the nanograined structure in Figure 1.

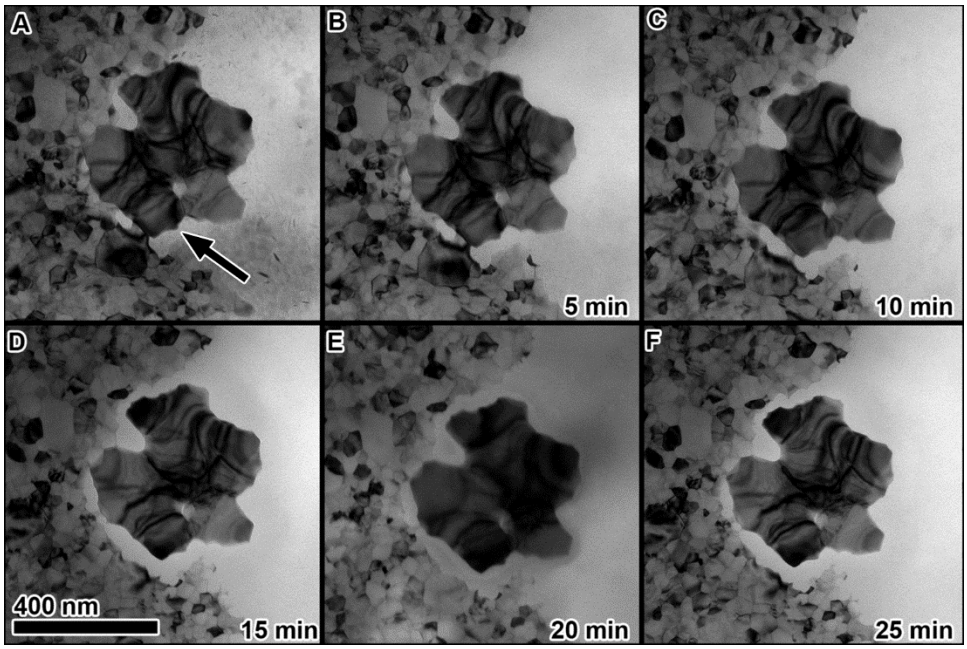

Figure 4: Dissolution of grains surrounding an abnormally large grain. A shows the initial observation of the area, and B-F demonstrate how the material surrounding the abnormal grain is dissolved leaving it isolated. A small protrusion from the abnormal grain is highlighted by an arrow in A.

Discussion

The corrosion event sequence provides some insight as to the nature of the processes. Once initiated the corrosion event propagates rapidly but for a limited time, indicating that there is a large initial driving force for dissolution followed by a rapid reduction of the driving force as seen in both Figures 2 and 3. One possible mechanism for reducing the driving force is that a local surplus of Fe ions is produced by the dissolution of the film. These free Fe ions lower the driving force enough to stop or substantially slow dissolution to the point that the film stabilizes itself against further corrosion. Another possibility is that dissolution of the grains exposes parts of the Si_3N_4 window, which could passivate the local area and stop the dissolution reaction. This is unlikely as Si_3N_4 shows good corrosion resistance against acids at low temperatures, including stronger acids such as H_2SO_4 [22], HCl [23, 24] and HF [23, 25].

The experiments also suggest that microstructural heterogeneities play a large role in dictating the propagation of corrosion fronts. This is clearly visible in the annealed films where large grains were impervious to attack but the small grains surrounding them had a higher level of susceptibility to corrosion than the surrounding matrix. Experiments by Horton *et al*. showed that the corrosion attack rate of FePd in 1 M HCl solution could be related to the surface orientations, with close-packed surfaces experiencing the least corrosion [26]. Previous work on grain growth in PLD nanocrystalline Ni samples has shown that low-surface energy grains, which correspond to grains with close-packed surface planes, dominate the annealed microstructure [27]. These studies suggest that the corrosion resistance of the abnormal grains is related to their close-packed surface planes. As the grain orientations were not measured, this could not be verified.

The difference in susceptibility to corrosion between the as-deposited and annealed samples is also interesting to note. Previous studies on PLD Ni have suggested that the grain boundaries in the as-deposited samples have a high free-volume content [28]. During annealing, these boundaries are replaced by lower-energy boundaries, with much of the grain boundary free volume transferring to grain interiors. Previous studies on corrosion behavior have shown that lower energy grain boundaries are more resistant to attack than higher energy grain boundaries [29-33], suggesting that the decrease in grain boundary energy in the annealed films along with the lower surface energies could account for the increased resistance to corrosion.

Electron beam-specimen interactions could accelerate the corrosion reaction either by increasing the kinetics of the reaction or by changing the reaction potential. Beam heating effects inside the liquid cell are currently unquantified but could account for a significant increase in reaction kinetics. In other systems, beam heating has caused over 100°C localized temperature increases [34]. Many systems experience increased corrosion rates at higher temperatures due to both film breakdown and faster ion transport. In addition, radiolysis of water and the acetic compound could break down the solution into H^+ and OH^- radicals, effectively increasing the concentration of the acid and making it more corrosive to the film. These variables are theoretically measurable during the *in situ* experiments and future studies to determine their contribution could provide more clarity into the corrosion process.

Conclusions

We have demonstrated that it is possible to use a microfluidic stage to directly view the effects of corrosion in Fe with nanometer resolution TEM. The dissolution of the as-deposited Fe film occurred both by discrete events wherein localized groups of grains dissolved and by larger-scale events where corrosion fronts propagated through hundreds of grains. Annealing the film on the substrate resulted in drastically reduced corrosion rates, potentially due to lower surface and grain boundary energies in comparison to the as-deposited films.

Acknowledgements

The authors gratefully acknowledge S. Hoppe for assistance with microfluidic stage and D. Bufford for assistance in analyzing the frame rates with the TViPs software. Sandia National Laboratories is a multi-program laboratory managed and operated by Sandia Corporation, a wholly owned subsidiary of Lockheed Martin Corporation, for the U.S. Department of Energy's National Nuclear Security Administration under contract DE-AC04-94AL85000.

1. Nagayama, M.i. and M. Cohen, *The Anodic Oxidation of Iron in a Neutral Solution: I . The Nature and Composition of the Passive Film.* Journal of The Electrochemical Society, 1962. **109**(9): p. 781-790.
2. Foley, C.L., J. Kruger, and C.J. Bechtoldt, *Electron Diffraction Studies of Active, Passive, and Transpassive Oxide Films Formed on Iron.* Journal of The Electrochemical Society, 1967. **114**(10): p. 994-1001.
3. O'Grady, W.E. and J.O.M. Bockris, *Interpretation of Mössbauer spectra of passive films on metals.* Surface Science, 1973. **38**(1): p. 249-251.
4. Kuroda, K., et al., *Electron Diffraction Study of the Passive Film on Iron.* Journal of The Electrochemical Society, 1982. **129**(10): p. 2163-2169.

5. Toney, M.F., et al., *Atomic Structure of the Passive Oxide Film Formed on Iron.* Physical Review Letters, 1997. **79**(21): p. 4282-4285.
6. Li, J. and D.J. Meier, *An AFM study of the properties of passive films on iron surfaces.* Journal of Electroanalytical Chemistry, 1998. **454**(1–2): p. 53-58.
7. Davenport, A.J., et al., *The Structure of the Passive Film That Forms on Iron in Aqueous Environments.* Journal of The Electrochemical Society, 2000. **147**(6): p. 2162-2173.
8. Gu, B., et al., *The in-situ TEM observation of corrosion facilitating dislocation emission, multiplication and motion for brass.* Scripta Metallurgica et Materialia, 1995. **32**(4): p. 637-640.
9. Gao, K.-W., et al., *In-situ TEM observation of dissolution-enhanced dislocation emission, motion and the nucleation of SCC for Ti□24Al□11Nb alloy in methanol.* Scripta Materialia, 1997. **36**(2): p. 259-264.
10. Li, J.X., et al., *In situ TEM study of stress corrosion cracking of austenitic stainless steel.* Corrosion Science, 2003. **45**(7): p. 1355-1365.
11. Zhou, G. and J.C. Yang, *Temperature effect on the Cu2O oxide morphology created by oxidation of Cu(0 0 1) as investigated by in situ UHV TEM.* Applied Surface Science, 2003. **210**(3–4): p. 165-170.
12. Zhou, G. and J.C. Yang, *Temperature effects on the growth of oxide islands on Cu(1 1 0).* Applied Surface Science, 2004. **222**(1–4): p. 357-364.
13. Malladi, S., et al., *Localised corrosion in aluminium alloy 2024-T3 using in situ TEM.* Chemical Communications, 2013. **49**(92): p. 10859-10861.
14. Chee, S.W., et al., *Studying localized corrosion using liquid cell transmission electron microscopy.* Chemical Communications, 2015. **51**: p. 168-171.
15. De Jonge, N. and F.M. Ross, *Electron microscopy of specimens in liquid.* Nature Nanotechnology, 2011. **6**(11): p. 695-704.
16. Klein, K.L., I.M. Anderson, and N. De Jonge, *Transmission electron microscopy with a liquid flow cell.* Journal of Microscopy, 2011. **242**(2): p. 117-123.
17. Woehl, T.J., et al., *Experimental procedures to mitigate electron beam induced artifacts during in situ fluid imaging of nanomaterials.* Ultramicroscopy, 2013. **127**: p. 53-63.
18. Zheng, H., et al., *Nanocrystal Diffusion in a Liquid Thin Film Observed by in Situ Transmission Electron Microscopy.* Nano Letters, 2009. **9**(6): p. 2460-2465.
19. Bruce D. Craig, E., *Handbook of Corrosion Data*. 1989, Metals Park, OH: ASM International.
20. Philip A. Schweitzer, P.E., *Metallic Materials: Physical, Mechanical and Corrosion Properties*. 2003, Marcel Dekker, Inc.: New York, New York.
21. Haynes, W.M., *CRC Handbook of Chemistry and Physics, 94rd Edition*. 2013: Taylor & Francis.
22. Monteverde, F., et al., *Corrosion of silicon nitride in sulphuric acid aqueous solution.* Corrosion Science, 2001. **43**(10): p. 1851-1863.
23. Sharkawy, S.W. and A.M. El-Aslabi, *Corrosion of silicon nitride ceramics in aqueous hcl and hf solutions at 27–80°C.* Corrosion Science, 1998. **40**(7): p. 1119-1129.
24. Sato, T., et al., *Corrosion of Silicon Nitride Ceramics in Aqueous Hydrogen Chloride Solutions.* Journal of the American Ceramic Society, 1988. **71**(12): p. 1074-1079.
25. Sato, T., et al., *Corrosion of silicon nitride ceramics in aqueous HF solutions.* Journal of Materials Science, 1988. **23**(10): p. 3440-3446.
26. Horton, D.J., A.W. Zhu, and J.R. Scully, *Crystallographic controlled dissolution and surface faceting in disordered face-centered cubic FePd.* MRS Communications, 2014. **4**: p. 113-119.
27. Kacher, J., et al., *Study of rapid grain boundary migration in a nanocrystalline Ni thin film.* Materials Science and Engineering A, 2011. **528**(3): p. 1628-1635.

28. Hattar, K., et al., *Defect structures created during abnormal grain growth in pulsed-laser deposited nickel.* Acta Materialia, 2008. **56**: p. 794-801.
29. Palumbo, G., et al., *Grain boundary design and control for intergranular stress-corrosion resistance.* Scripta Metallurgica et Materialia, 1991. **25**(8): p. 1775-1780.
30. Lehockey, E.M., et al., *On improving the corrosion and growth resistance of positive Pb-acid battery grids by grain boundary engineering.* Journal of Power Sources, 1999. **78**(1–2): p. 79-83.
31. Shimada, M., et al., *Optimization of grain boundary character distribution for intergranular corrosion resistant 304 stainless steel by twin-induced grain boundary engineering.* Acta Materialia, 2002. **50**(9): p. 2331-2341.
32. Komotori, J., et al., *Corrosion response of surface engineered titanium alloys damaged by prior abrasion.* Wear, 2001. **251**(1–12): p. 1239-1249.
33. Palumbo, G., E.M. Lehockey, and P. Lin, *Applications for grain boundary engineered materials.* JOM, 1998. **50**(2): p. 40-43.
34. Howe, J.M., et al., *Effects of heat and electron irradiation on the melting behavior of Al–Si alloy particles and motion of the Al nanosphere within.* Journal of Electron Microscopy, 2004. **53**(2): p. 107-114.